

Innovations in the Data Processing Algorithm for Chinese FY Meteorological Satellites

XU Jianmin (许健民), GUO Qiang* (郭强), LU Qifeng (陆其峰), LU Feng (陆风),
and ZHANG Xiaohu (张晓虎)

National Satellite Meteorological Center, China Meteorological Administration, Beijing 100081

(Received April 29, 2014; in final form August 7, 2014)

ABSTRACT

This study introduces some innovations in the data processing algorithm for Chinese FY meteorological satellites. Issues about satellite image navigation, radiation calibration, and data assimilation are discussed.

A time series of the earth's disk center-line count provides information on the orientation of the satellite spin axis. With this information, the altitude parameters of the satellite and then the earth disk location in the south-north direction may be solved. In each spin cycle, the satellite views the sun and the earth. Given the satellite position and altitude, the angle (β) subtended at the satellite by the sun and the earth can be calculated and predicted. Thus, the earth's disk location in the east-west direction is fixed. Based on this principle, we derived an automatic image navigation algorithm for FY2 geosynchronous meteorological satellites with an accuracy approaching pixel level.

The FY2 meteorological satellite traveling in a geostationary orbit suffers a large amount of radiation from the sun. The radiation varies on both diurnal and annual scales, which causes radiation responses in the thermal infrared (IR) bands wherein the wavelengths greater than $3.5\ \mu\text{m}$ vibrate periodically on scales of hours to years. These vibrations must be precisely calibrated. First, based on the accurate estimation of the radiant contribution from the front-optics, the variation characteristics of the calibration parameters are obtained on a temporal scale of hours from the space-borne inner-blackbody (IBB) measurement results. Second, the in-orbit measured radiation of the lunar surface is referenced and utilized to correct the systematic bias of the IBB calibration from daily to annual scales. By using such algorithms, we achieved a calibration accuracy of the FY2 satellite's IR imagery of less than 1 K.

The on-orbit satellite instrument parameters play an important role in data quality; however, they may be mis-measured due to limitations in the measurement conditions or may be changed due to the space environment after launch. A satellite instrument parameters on-orbit optimizer (SIPOn-Opt) for a polar orbit meteorological satellite was developed to optimize the true state of the instrument parameters on-orbit with regard to the observation constraints. When applying the SIPOn-Opt to FY3 sounding instruments, the FY3 data quality was much improved, compared to its European and the U.S. polar orbit meteorological satellite counterparts, leading to improved forecast skill of numerical weather prediction.

Key words: meteorological satellite, data processing algorithm, image navigation, radiation calibration, data assimilation

Citation: Xu Jianmin, Guo Qiang, Lu Qifeng, et al., 2014: Innovations in the data processing algorithm for Chinese FY meteorological satellites. *J. Meteor. Res.*, **28**(5), 948–964, doi: 10.1007/s13351-014-4034-2.

1. Introduction

China's meteorological satellite program was initiated in the 1970s. Over the past 40 years, 13 meteorological satellites have been developed. The polar and geostationary series satellites, known as Fengyun-1 (3)

(FY1(3)) and Fengyun-2 (FY2), respectively, are in current operation. They are ranked by the World Meteorological Organization as being part of the World Weather Watch space component. After the launch of these satellites, the ground station has responsibility for the management and utilization of the satellite

Supported by the National Natural Science Foundation of China (40275007, 41275036, 40971200, 41075019, 41275034, 91338203, and 40705037), China Meteorological Administration Special Public Welfare Research Fund (GYHY201206002), Ministry of Finance (201306001), and Ministry of Science and Technology of China (863-2003AA133050 and 2012AA120903).

*Corresponding author: guoqiang@cma.gov.cn.

©The Chinese Meteorological Society and Springer-Verlag Berlin Heidelberg 2014

system, including data receiving, processing, and application (Xu et al., 2006). This study introduces innovations in the data processing algorithm for the Chinese FY meteorological satellites.

The radiometer onboard the FY2 meteorological satellite senses atmospheric and earth objects remotely in pixel format. The obtained data are then processed at the ground station. Data processing includes image navigation, radiation calibration, and product generation and assimilation. Image navigation yields information on the location of the observed objects. Radiation calibration indicates the amount of radiation received from the observed objects by the satellite. Data assimilation helps to improve numerical weather prediction. This study uses these three measures to describe the innovations in the FY data processing algorithm.

Section 2 introduces the FY2 image navigation algorithm (Lu et al., 2008). As a geosynchronous meteorological satellite, FY2 makes its observations with 5-km infrared (IR) or 1.25-km visible resolution and angular resolutions of 140 and 35 μ rad at an orbit 36000 km above the earth's surface. Although it is called a geostationary satellite, in reality, the position and altitude of the satellite vary. The FY2 image navigation algorithm does not use the traditional land mark matching technique. In fact, a time series of the earth's disk center-line count and the angle subtended at the satellite by the sun and earth provide accurate information on the altitude and misalignment parameters of the satellite. With this information, pixel-level image navigation and minor animation shifts in the geostationary orbit may be addressed.

Section 3 introduces the radiometric calibration algorithm for the FY2 geostationary meteorological satellite, which contains two main components, i.e., inner-blackbody (IBB) calibration and lunar calibration for in-orbit conditions. In particular, the diurnal variation in the frequency of the radiometric response in the IR band and the annual systematic variation of the IBB calibration are solved and successfully applied in currently operating satellites 2D, 2E, and 2F. The accuracy of the calibration results is high, reaching levels better than 1 K.

Section 4 introduces the satellite instrument parameters on-orbit optimizer (SIPOn-Opt). It is widely assumed that meteorological satellite on-orbit instruments are consistent with their design, that the instrumental performance parameters on-orbit are consistent with the values measured before the satellite is launched, and that even if certain differences exist, there is no effective way to calculate such values. An SIPOn-Opt for the polar orbit meteorological satellite was developed to optimize the true state of the instrument parameters on-orbit with respect to the observational constraints, and to help diagnose and correct the dominant observing system biases in the satellite data preprocessing system. When applying SIPOn-Opt to the FY3 sounding instruments, the FY3 data are much improved compared with data from its counterparts, the European and the U.S. polar orbit meteorological satellites, and the forecast skill of the numerical weather prediction model is also improved (Lu et al., 2011a, b, 2012). When the SIPOn-Opt is applied to meteorological satellite instruments (MSU and AMSU-A) from Europe and the U.S., the quality and effectiveness of their data in applications over the past 40 years are also improved (Lu et al., 2014).

Section 5 summarizes these major innovations in the data processing algorithm for FY satellite data processing.

2. Image navigation algorithm for FY2 geosynchronous meteorological satellites

2.1 *The earth disk location in the south-north direction*

An ideal spin-stabilized geostationary meteorological satellite should have a round orbit on the equatorial plane with its spin axis parallel to the earth's rotation axis. When those conditions are satisfied, the images observed are nominal without any animation shifts. In reality, these conditions are never satisfied. The real orbit and altitude show a minor departure from the nominal ones. In a geostationary orbit, however, these minor deviations in orbit and altitude have an negligible influence on image navigation.

A time series of the earth's disk center-line cou-

nts, namely the north-south movement of the earth's disk in the image during 7–8 June 2006 is shown in Fig. 1a. The movement appears as a simple sinusoidal function. The behavior of the line counts is well repeated. When the image origins are placed at the first line and column and then rendered as an image animation, the earth's disk shifts in the north-south direction one cycle each day. When the image origins are placed at the earth's disk center and then rendered into an image animation, the earth's disk swings both clockwise and counterclockwise one cycle each day. In Fig. 1b, the sinusoidal function is simulated with the data during 7–8 June 2006 (black dots) and is then extended to 9 June 2006 (hollow dots). The good overlap of the hollow dots on the extension of the sinusoidal curve shows that the earth's disk center-line count is predictable.

The phenomena described above reflect the impact of the satellite altitude on the imaging process. Viewed from a spin geosynchronous satellite, the earth's disk location passes through a diurnal cycle. This phenomenon is schematically illustrated in Fig. 2, which presents the FY2 observation geometry. In an ideal situation, the spin axis of the satellite is parallel to the earth's axis of rotation. In practice, this

situation is never achieved. As shown in Fig. 2, at 0600 (1800) UTC, the satellite looks up (down) at the earth, and the earth's disk is in the downward (upward) side of the image. Around these two moments, the earth's disk center is displaced mostly in the north-south direction, and the images turn only slightly in a day. At 0000 (1200) UTC, the earth's disk is minimally displaced, but the scan lines deflect the greatest amount, and the turning of the images is greatest in a single day. At 0000 (1200) UTC, the satellite views the earth with its spin axis turning clockwise (counterclockwise), while the image turns counterclockwise (clockwise).

Observation vectors can be measured on the observation images, as shown in Fig. 3, where E is the earth center and S is the satellite. On the line from S to E, make a normal plane "image" through F with origin O. F is at the central column. SO is perpendicular to the plane "image". The trajectory of the scan lines across the plane "image" forms the observation image. The 1250th scan line passes through C. C is the cross-point of the 1250th line and the central column. Assume vector \mathbf{S}_E is from S pointing to E and vector \mathbf{S}_Y is the spin vector of the satellite. On the plane consisting of vectors \mathbf{S}_E and \mathbf{S}_Y , there is another vector, \mathbf{S}_Z ,

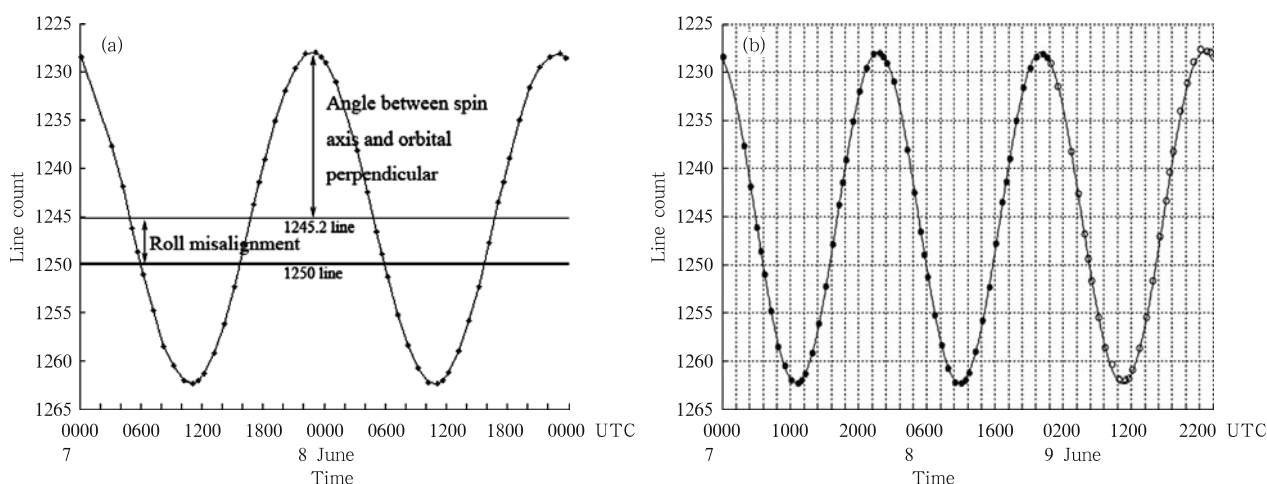


Fig. 1. Time series of the earth's disk center-line count for FY2C during (a) 7–8 and (b) 7–9 June 2006. The ordinate is the earth's disk center-line count (increasing downward), the abscissa is the time (UTC). Black dots represent the previous earth disk center-line counts for 7–8 June 2006 on which the simulation and extension are based, the curve is the simulation and extension of the earth disk center-line counts, and hollow dots are the future observations of the earth disk center-line counts for 9 June 2006, which are independent of the extension of the curve. [From Lu et al., 2008]

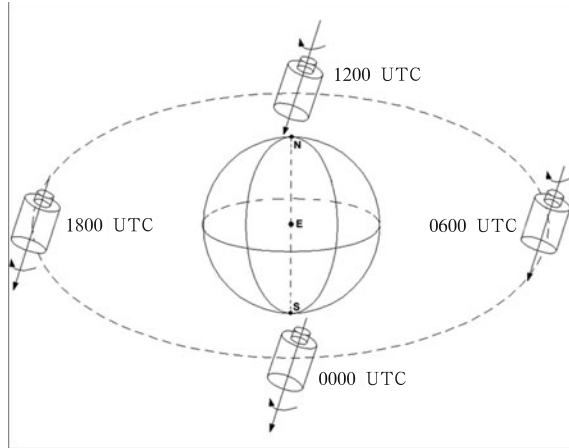


Fig. 2. FY2 observation geometry. N is the Arctic, E is the earth's center, and S is the Antarctic. The line linking the Arctic and Antarctic is the earth's rotation axis. The spin axis of the satellite is also shown. [From Lu et al., 2008]

perpendicular to the plane “image”. Vector \mathbf{S}_Z passes through S and O. The angle subtended at satellite S by vectors \mathbf{S}_E and \mathbf{S}_Z can be measured by $\theta + \rho + \frac{\pi}{2}$. Then, the observation equation is established as follows:

$$\mathbf{S}_E \cdot \mathbf{S}_Y = \sin(\theta + \rho). \quad (1)$$

Equation (1) with 0 pitch misalignment ρ was originally expressed by Hambrick and Phillips (1980; abbreviated as HP80 hereafter). In Eq. (1), \mathbf{S}_E , θ , and ρ can be measured on the observation image. The spin vector (altitude) of the spin satellite, \mathbf{S}_Y , is then solved from Eq. (1).

In addition to the altitude of the satellite, misalignment of the visible IR spin-scan radiometer (VISSR) from the satellite should also be considered. Figure 4 is a schematic diagram of this misalignment. For an ideal spin meteorological satellite, the 1250th line should scan out a plane. In reality, due to the misalignment shown in Fig. 4b, the 1250th line scans out a cone. The angle between the cone and the spin plane is the ρ component of the misalignment. It can be verified that the ρ component of the misalignment is related to the deviation of the image in the north-south direction and is also the solution of Eq. (1). With Eq. (1), the earth disk location in the south-north direction is fixed.

2.2 The earth disk location in the east-west direction

Spin geosynchronous meteorological satellites use

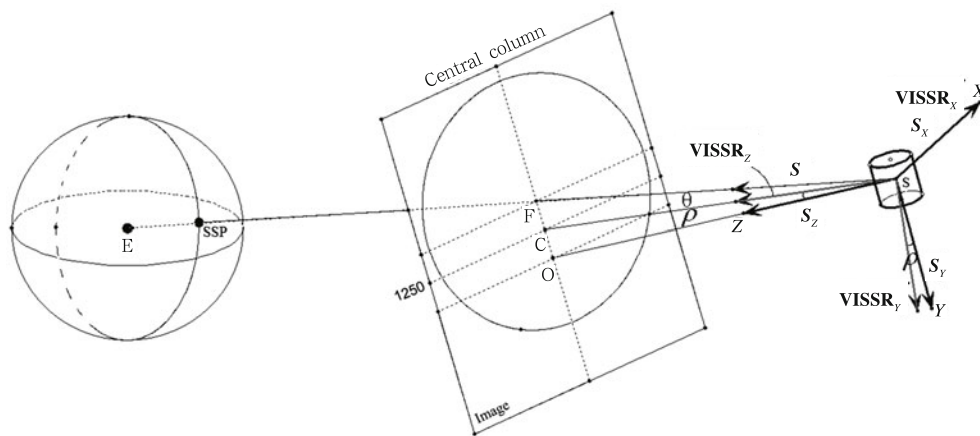


Fig. 3. The satellite coordinate system. E is the earth center and S is the satellite, \mathbf{S}_Y matches the spin axis of the satellite, and the SZX plane is the spin plane of the satellite. The earth center E and the satellite spin axis make up the SYE plane. The SYE plane crosses the satellite spin plane (SZX) to form the Z axis. Normally, the axis does not extend toward the earth center but is in the plane defined by the Earth center and the satellite spin axis \mathbf{S}_Y . The \mathbf{S}_X axis is defined by $\mathbf{S}_Y \times \mathbf{S}_Z = \mathbf{S}_X$. Take a point O along the line extended from the vector \mathbf{S}_Z . Make a plane IMAGE O, which is perpendicular to \mathbf{S}_Z . The earth is projected on the IMAGE plane to form the observation image. On the projected plane IMAGE, the earth center E is at F. The 1250th scan line crosses the central column of the plane IMAGE at C, which is the center of the observation image. [After Hambrick and Phillips, 1980]

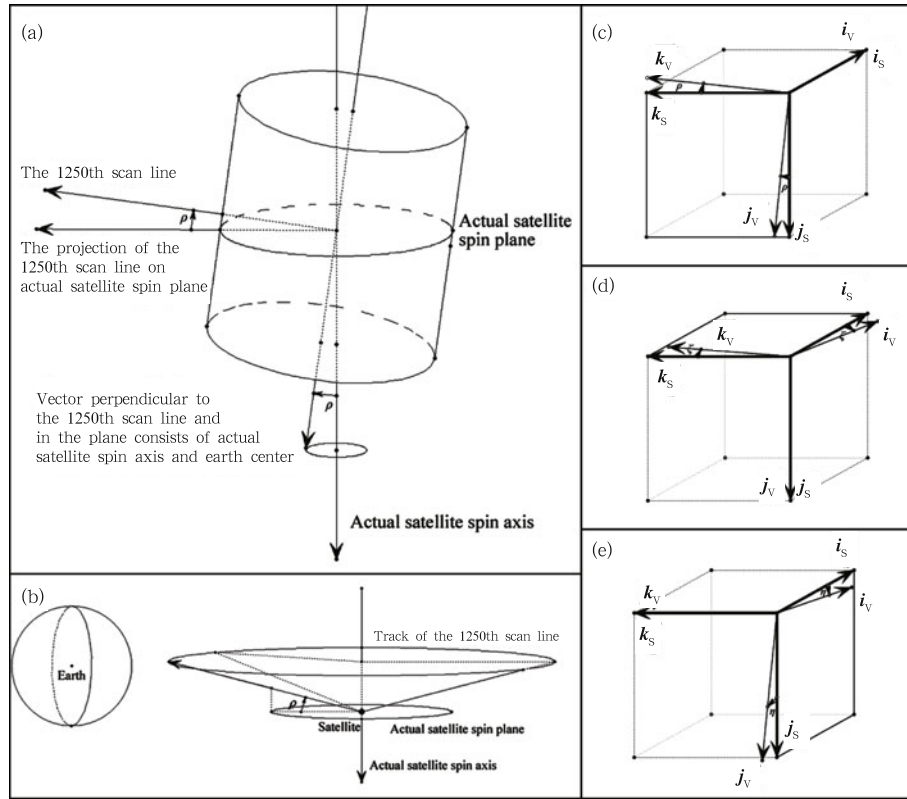


Fig. 4. Schematic diagrams demonstrating the misalignment of the FY2 visible IR spin-scanning radiometer (VISSR). (a) Difference between the actual VISSR and the ideal; (b) impact of roll misalignment on the imaging process; (c) misalignment of the roll component; (d) misalignment of the yaw component; and (e) misalignment of the pitch component. [From Lu et al., 2008]

a sun sensor installed on the side face of the satellite to control the pointing of the VISSR to the earth and to align the scan lines. Based on an accurate sun position and the angle subtended at the satellite by the sun and earth (β), individual scan lines are aligned, resampled, and registered at the ground station, and observation images are assembled. Figure 5 is a schematic diagram of the β angle geometric formulation. In Fig. 5a, \mathbf{S}_Y is the spin axis of the satellite, $\mathbf{S}_{\text{earth}}$ is the vector pointing from the satellite to the earth's center, and \mathbf{S}_{sun} is the vector pointing from the satellite to the sun. Here, we define the following three planes, i.e., the S plane consisting of the spin axis and the sun, the E plane defined by the spin axis and the earth, and the P plane passing through the satellite and perpendicular to the satellite spin axis. Note that $\mathbf{S}_Y \times \mathbf{S}_{\text{sun}}$ and $\mathbf{S}_Y \times \mathbf{S}_{\text{earth}}$ are perpendicular to the vectors \mathbf{S}_{sun} and $\mathbf{S}_{\text{earth}}$ projected at the satellite spin plane, respec-

tively. The β angle can be written as follows:

$$\beta = \cos^{-1} \left[(\mathbf{S}_Y \times \mathbf{S}_{\text{sun}}) \cdot (\mathbf{S}_Y \times \mathbf{S}_{\text{earth}}) \right]. \quad (2)$$

Here, β is a significant parameter for observation by spin-stabilized geosynchronous meteorological satellites. In Eq. (2), vectors \mathbf{S}_{sun} and $\mathbf{S}_{\text{earth}}$ are related to satellite position and \mathbf{S}_Y to altitude. When the satellite position and altitude are well predicted, angle β can be accurately calculated. The value thresholds of β are from 2π to 0. At a time near local midnight, when the sun, earth, and spin axis of the satellite share a common plane, β is given a value of 2π . The value of β decreases monotonically until a time near the next local midnight when it approaches 0, as shown in Figs. 5b and 5c. With the addition of Eq. (2), the navigation model becomes complete, and a fully automatic solution of the equations is realized.

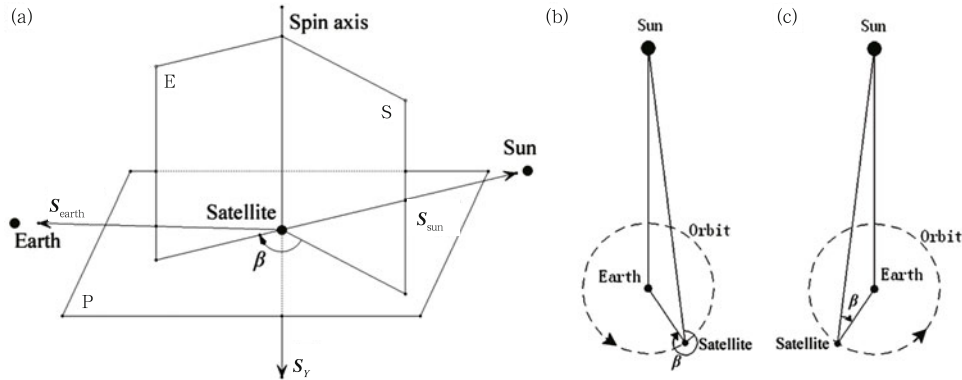


Fig. 5. A schematic diagram illustrating the β angle. (a) Three-dimensional view, (b) plane view after local midnight, and (c) plane view after local noon. [From Lu et al., 2008]

2.3 Completely closed coordinate and parameter systems

To express the basic principle for FY2 image navigation, the above equations have been simplified. In practice, within a 25-min time period during which FY2 takes a full disk image of the earth, the observation object (earth), the observation tool (satellite), and the sun that is used to align the satellite scan lines to point them at earth, are all in motion. Accurate image navigation requires the knowledge of the position of these three objects, the altitude of the satellite, and the misalignment of the VISSR relative to the satellite. Completely closed coordinate and parameter systems are essential.

The parameters are defined and applied in the coordinate systems with a clear geometric meaning. In the defined coordinate systems, the parameters may not be conservatory with time. Thus, the parameters must be defined according to the conservatory coordinate systems. The navigation equations should be solved by using the conservatory coordinate systems. To make the transformation from the defined to the conservatory coordinate systems, a series of intermediate coordinate systems are necessary. Correct parameter definition and transformation among different coordinate systems are essential for solving image navigation equations.

2.4 Image navigation results

Figure 6 shows observation images overlaid with

latitude-longitude grids, coastlines, and other geographical features from FY2C visible images at 0456 UTC 8 June 2006. The resolution for the visible channel is four times better than that of the IR channel. The coast lines overlaid on the images are predicted ones. Figure 6a is a full disk image, while the others are local section images with raw visible resolution. To show detail, the image pixel size in the local section images is zoomed to 10 times larger than the geographical feature size. These images clearly show a good overlap between images and grids.

3. Radiometric calibration algorithm for the FY2 geostationary meteorological satellite

3.1 Lunar calibration for the IR band

Traditionally, there are two main calibration methods operationally utilized for FY2, i.e., vicarious in-situ calibration using simultaneous observations from space-borne and on-ground instruments and inter-calibration of observations between different on-orbit sensors. Vicarious in-situ calibration has high accuracy for validation but a relatively small dynamic range of the target's radiation. Inter-calibration is a stable method but is highly dependent on the spatial matching procedure. In addition, the target earth is inevitably influenced by the atmospheric radiation correction in both the in-situ and the inter-calibration methods. Therefore, there is a growing demand for a new calibration method that has stable performance in its radiation characteristics to overcome the limita-

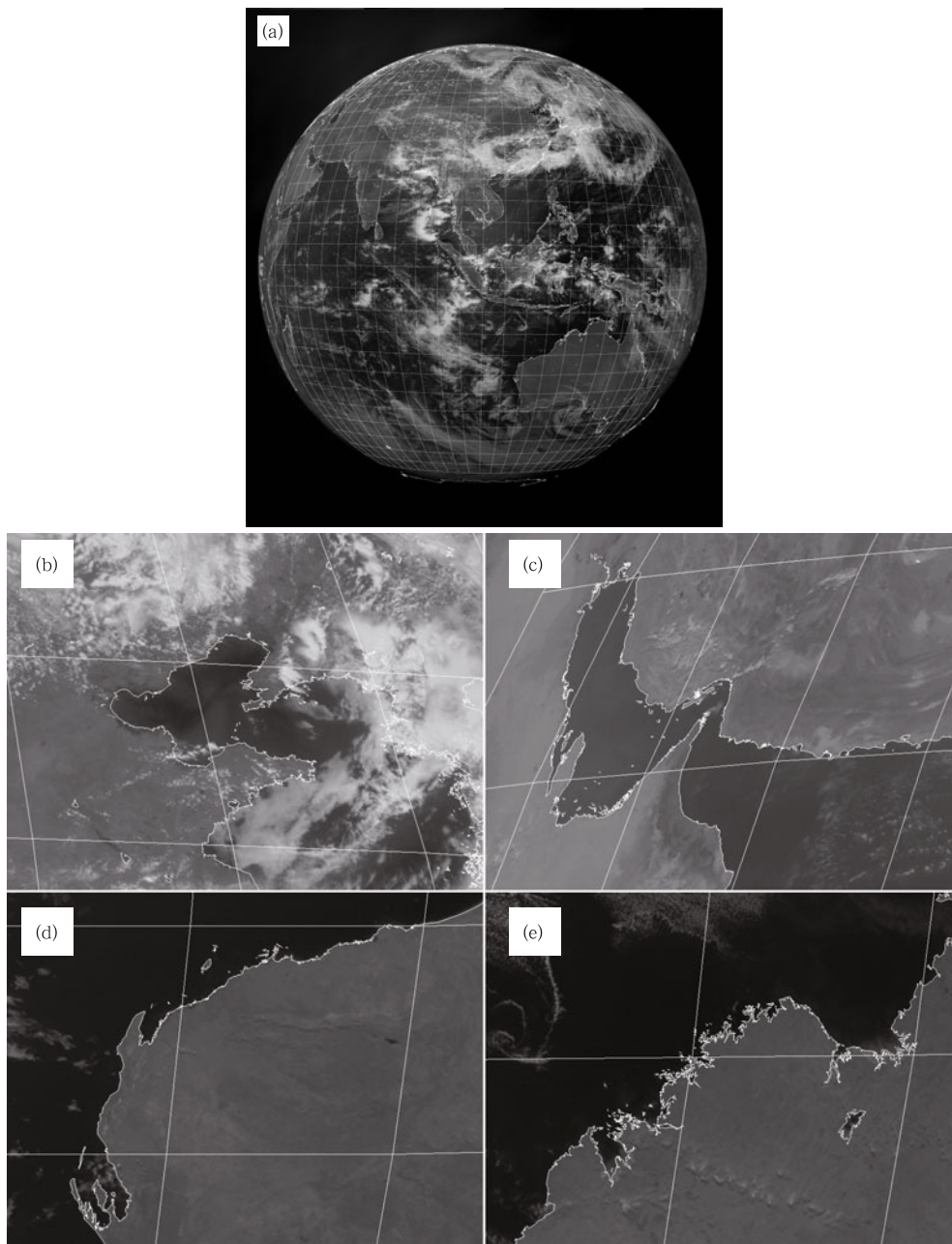


Fig. 6. Full-resolution FY2C visible images with superimposed coastal lines showing the FY2 image navigation results. (a) Full disk image of FY2C at 0456 UTC 8 June 2006. (b)–(e) Image sections of FY2C at 0456 UTC 8 June 2006. [Adapted from Lu et al., 2008]

tions of the existing methods.

The photometric stability of the lunar surface can reach 10^{-9} per year, and is widely used as the reference source for space-borne sensor calibration in free space. Outside China, lunar calibration in the visible band has been conducted, but IR band lunar calibration is rarely reported. The main difficulty lies in modeling

the nonthermal, nonuniform, and nongray body characteristics of the lunar surface for IR lunar calibration (Guo et al., 2012). Moreover, results from astronomic calculations indicate that lunar calibration in the IR band cannot completely meet the high frequency requirements of on-orbit operational calibration. In fact, it is merely useful for the systematic error adjustment

of a space-borne sensor's radiometric response. A typical on-orbit lunar image observed by FY2F is shown in Fig. 7a, whereas Figs. 7b and 7c show images after compensation for the relative movement between the moon and the satellite. These images are ultimately used for on-orbit lunar calibration in the IR band.

In ordinary blackbody calibration, when describing the incident radiance to the sensors, it is critical that the blackbody's temperature and its distribution field be measured as accurately as possible. However, the lunar surface temperature cannot be measured in real time. The temperatures of targets illuminated by the sun on the lunar surface are usually higher than 300 K, and using the existing lunar surface temperature estimation model, with its accuracy of about 1.5–2.0 K, is unacceptable for real radiometric calibration in the IR bands. Therefore, one of the kernel-level technologies in FY2's operational calibration is the introduction of the equivalent dual-band emissivity ratio, which is independent of the temperature of the lunar surface's uniform targets, based on the modeling of the observed radiance from the moon. This ratio establishes a quantitative relationship between the observed radiances from different thermal IR bands. The lunar calibration equation between two IR bands is further deduced as follows:

$$(a_{\text{IR1}})_{\text{moon}} \cdot f_{\text{moon}}(c_{\text{IR1}}) + (a_{\text{IR2}})_{\text{moon}} \cdot f_{\text{moon}}(c_{\text{IR2}}) = (b_{\text{IR1\&IR2}})_{\text{moon}}, \quad (3)$$

where $(a_{\text{IR1}})_{\text{moon}}$ and $(a_{\text{IR2}})_{\text{moon}}$ are the two constants related to the spectral response as well as the dynamic range, $(b_{\text{IR1\&IR2}})_{\text{moon}}$ is a variable determined by the on-orbit synchronous lunar observations in both the IR1 and IR2 bands, c_{IR1} and c_{IR2} are the two cali-

bration slope parameters to be solved in the IR1 and IR2 bands, respectively, and $f_{\text{moon}}(\cdot)$ is a known real function varying with the calibration slope. By using the results from in-lab calibration as well as introducing the relationships of the calibration parameters between different bands, the calibration slopes can be accurately solved with Eq. (3).

3.2 Absolute radiometric calibration with IBB calibration

Some theoretical analyses indicate that the calibration slope, which is the most important parameter to be determined in radiometric calibration, is mainly dominated by the normalized detectivity (D^*). To date, with the continuous development of the HgCdTe detector technique, photoconductive and photovoltaic detectors are used in most meteorological satellites worldwide. D^* values between 3.5 and 12.5 μm can reach the order of 10^{10} to $10^{11} \text{ Hz}^{1/2}\text{W}^{-1}$, finally realizing perfect background limitation detection performance. With this means, the variation in the instrument's background radiation will inevitably influence D^* and directly cause variation in the calibration slope parameter.

By using the FY2E satellite as an example, Fig. 8 shows the temperature variation in the VISSR's front-optics, represented by the primary mirror (red curve), the secondary mirror (blue curve), and the temperature variation in the VISSR's after-optics represented by the calibration mirror (green curve), where the maximal temperature difference approaches 20 K. It can be easily understood that the variation in background radiation due to the changing of environmental temperature should appear as an annual feature. Thus, the suitable radiometric reference and its cali-



Fig. 7. Typical on-orbit lunar images observed by FY2F. (a) Raw lunar image in the VIS band, (b) lunar image in the IR1 band after compensating for its movement relative to the satellite with spatial oversampling, and (c) lunar image in the IR1 band after compensating for its movement relative to the satellite with spatial ordinary sampling.

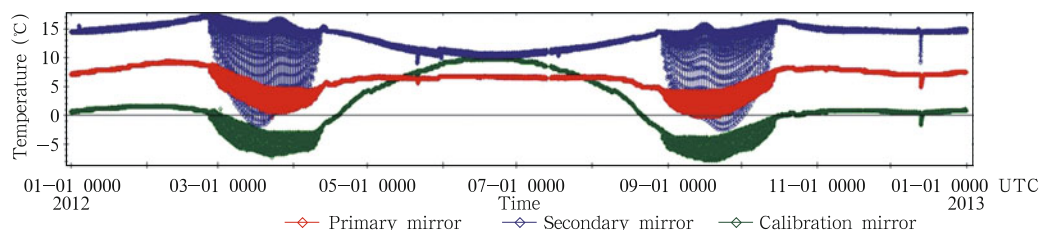


Fig. 8. Temperature variations of the main optical elements of the FY2E satellite during 2012.

ration method should have the capability to calibrate diurnal variations in the sensor's radiometric response. This is the key issue for achieving high accuracy calibration in IR bands for the FY2 satellite.

Figure 9 illustrates the theoretical contrast between the typical full-path blackbody (BB) calibration and the partial-path BB calibration (or the so-called inner-blackbody calibration; IBB). For both full-path and partial-path BB calibrations, there are ordinarily two steps, i.e., blackbody and cold-space observations, the difference between which is the valid BB observation. In particular, for full-path BB calibration, the switch between the two steps is realized by the rotation of the scanning mirror by about 90° , where both the front-optic and after-optic radiant influences are included, and the difference as a net BB observation can be directly used to determine the calibration parameter. For IBB, however, although the IBB can be observed by rotating the calibration mirror, the radiometric contribution of the calibration mirror is added to the IBB observation without the contribution of the front-optics. Therefore, the traditional full-path BB calibration method cannot be simply employed to deal with IBB observation. The

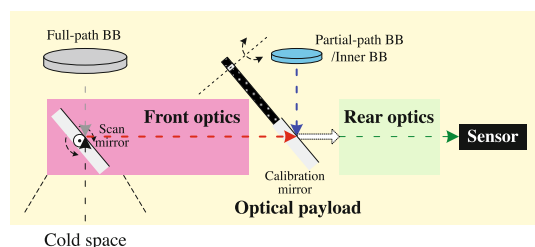


Fig. 9. Contrast between typical full-path and partial-path blackbody calibrations for optical remote sensing instruments.

key issue is how to accurately estimate the radiometric contributions of the front-optics as well as the calibration-optic component (FCC). For the operational calibration of FY2 satellites, we established a single-temperature IBB method with a radiometric contribution estimation model for the FCC, where telemetric information from multiple optical components specific infinite element modeling and in-lab calibration results are considered. The IBB equation is given by Eq. (4).

$$(c_{\text{slope}})_i = \frac{(k_{\text{equal}})_i}{(v_{\text{IBB}})_i + \sum_j (k_j)_i \cdot g_i(T_j)},$$

$$i \in \{\text{IR1, IR2, IR3, IR4}\}, \quad (4)$$

where j represents a real FCC, i.e., primary mirror, secondary mirror, folding mirror, calibration mirror, and delay lens for FY2; $g_i(T_j)$ is the modeled finite-element expression for the j th FCC; k_j is a coefficient determined by the material and shape of the corresponding FCC; k_{equal} is the equivalent IBB incident radiance, which can be estimated with in-lab results; and v_{IBB} is the IBB observation expressed as voltage.

3.3 Main achievements of radiometric calibration of the FY2 geostationary meteorological satellite

Figure 10 shows a real lunar calibration result for both the IR1 and IR2 bands of FY2E by using the lunar observations at 1000 UTC 1 January 2012. The metrics of the horizontal and vertical ordinates in Figs. 10b and 10c are voltage and radiance, respectively, and R2 approaches 0.99 with perfect performance. The calibration slopes, varying with the environmental

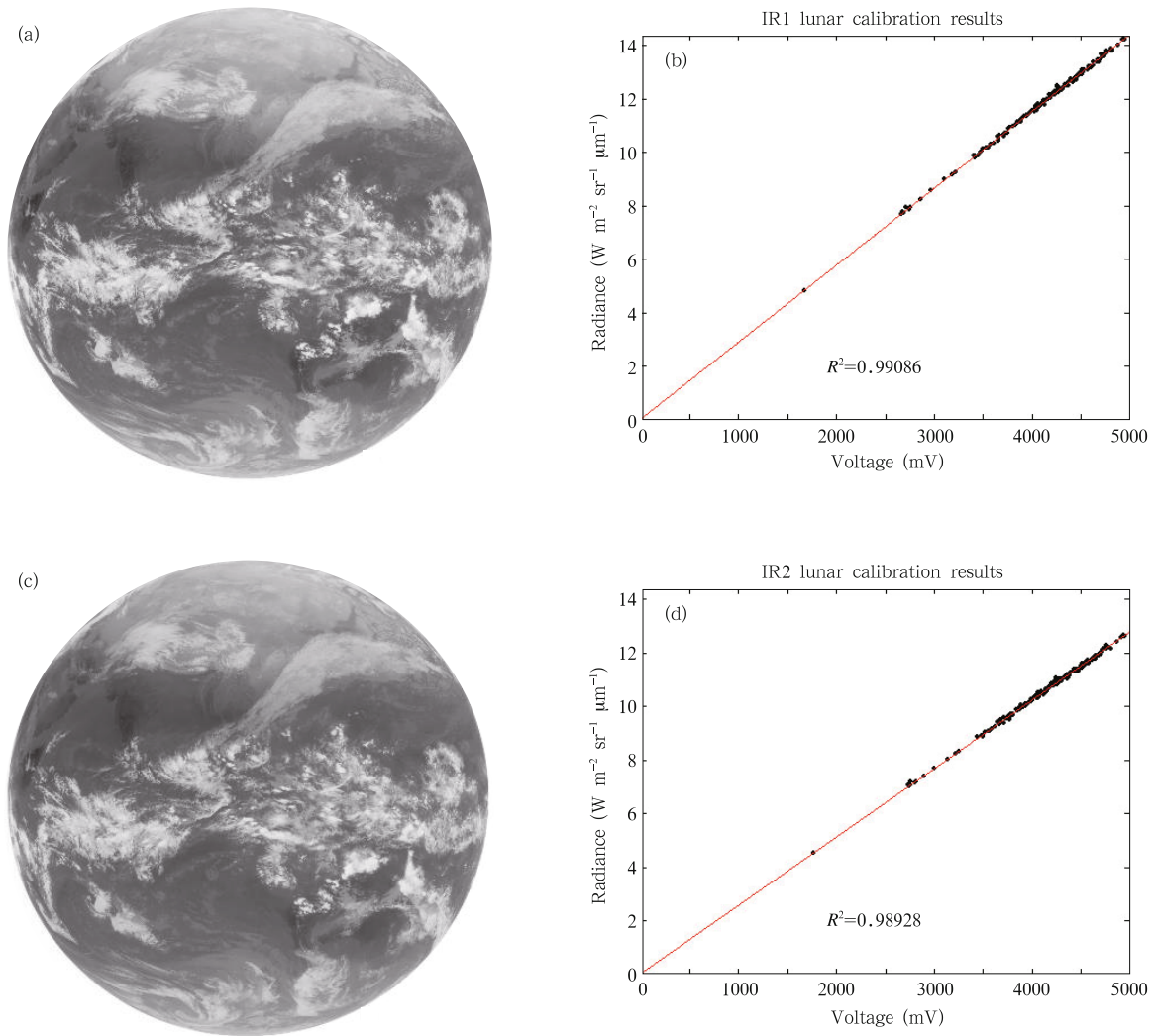


Fig. 10. Lunar calibration results of the FY2E satellite at 1000 UTC 15 January 2012. (a) Earth-disk image with moon in the IR1 band, (b) lunar calibration curve in radiance for the IR1 band, (c) earth-disk image with moon in the IR2 band, and (d) lunar calibration curve in radiance for the IR2 band.

temperatures before and after the satellite eclipses for both FY2E and FY2F, are shown in Figs. 11 and 12, respectively. Specifically, the horizontal coordinates of Figs. 11a and 11b are time. The vertical coordinate of Fig. 11a is temperature, and the vertical coordinate of Fig. 11b is slope (unit: $\text{W m}^{-2} \text{sr}^{-1} \mu\text{m}^{-1} \text{V}^{-1}$). In Fig. 11a, the green, blue, black, and red lines represent the temperatures of the delay lens, the primary mirror, the secondary mirror, and the calibration mirror, respectively. In Fig. 11b, the red, blue, black, and green lines represent the calibration slopes of IR1–IR4. Noticeably, during the satellite’s eclipse,

the calibration slopes of all the IR bands (IR1–IR4) are characterized by great diurnal variability. In the IR1 band, for example, the relative diurnal variation of the calibration slope can reach 3%. This equals a 3-K error when observing a target with a temperature of 300 K without any modification. Moreover, after the spring satellite eclipse, the calibration slope of all the VISSR’s IR bands rapidly increases day by day and reaches a peak around the summer solstice. This pattern is closely related to the increase in the satellite’s temperature and the decrease in its cooling capacity. It is clear that the FY2 satellite’s operational calibra-

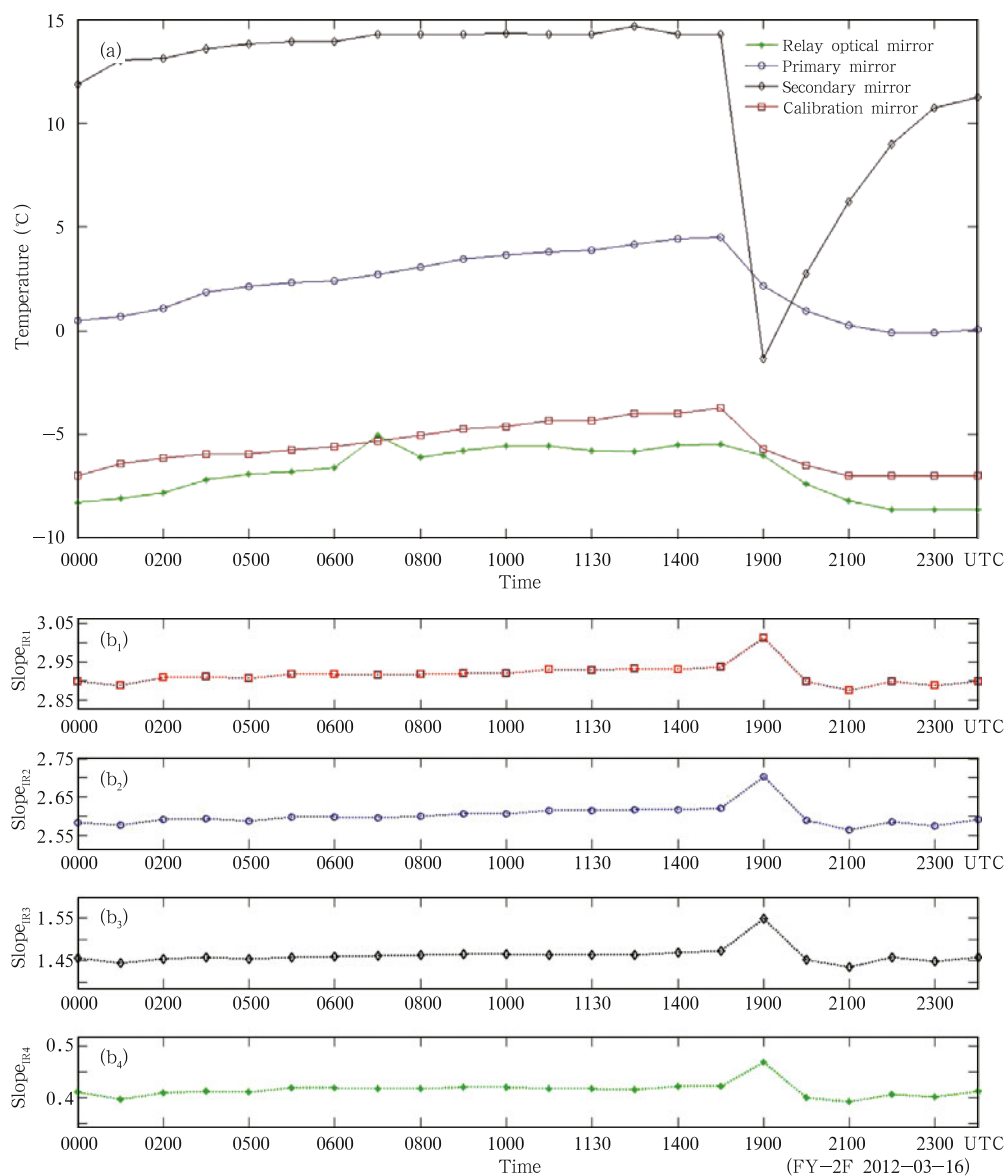


Fig. 11. Calibration slope's diurnal variations in environmental temperature in the IR1–IR4 bands for FY2F on 16 March 2012. (a) Temperature variations of the main optical elements and (b) calibration slope's diurnal variations in the IR1–IR4 bands.

tion results better describe the time-varying features of the calibration parameters for the on-orbit VISSR, which is the baseline of the proposed more highly accurate calibration of the inner-blackbody corrected by lunar emission (CIBLE) method (Guo et al., 2013). In Fig. 13, observations from the Infrared Atmospheric Sounding Interferometer (IASI) sensor under the framework of the global space inter-calibration system (GSICS) is used as a reference, and the calibration bias is evaluated at the high temperature segment

(290 K) for the FY2E IR1 band after April 2013 (Note: the CIBLE method has been used for FY2E since 27 March 2013). As shown in Fig. 13a, the total bias shows pretty good to be less than 1 K. Meanwhile, as shown in Fig. 13b, when the two high spectral sensors, i.e., the IASI and the Atmospheric Infrared Sounder (AIRS), are selected for reference, the relative difference in the results remains about zero, indicating that the assessment results of Fig. 13a are reliable.

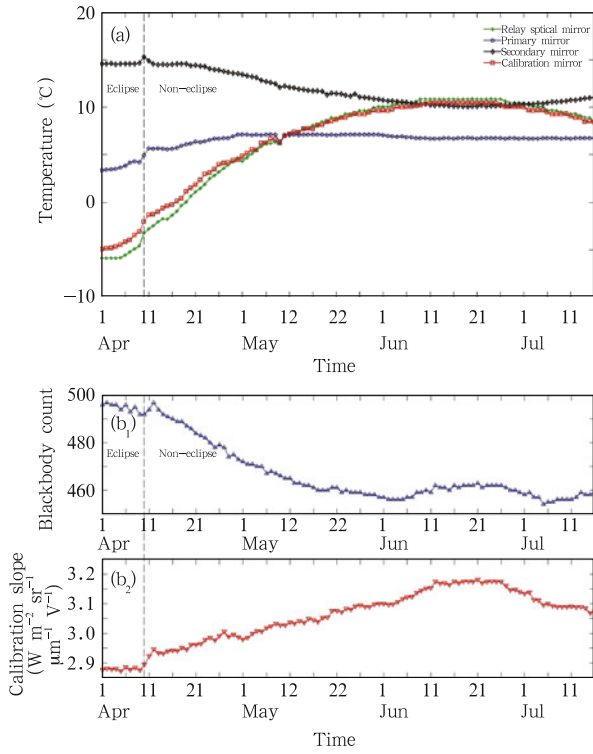


Fig. 12. Calibration slope's annual variations in environmental temperature in the IR1-IR4 bands of FY2F between April and July of 2012. (a) Temperature variations of the main optical elements and (b) blackbody counts and calibration slope's annual variations in the IR1-IR4 bands.

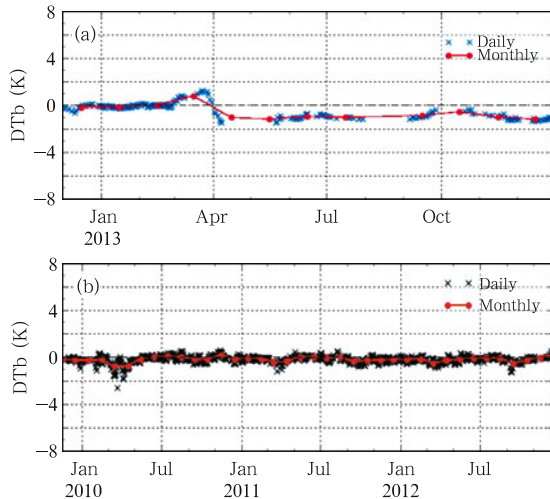


Fig. 13. Calibration accuracy evaluation results from the GSICS method for the FY2E IR1 band. (a) Calibration bias for the condition of the target's brightness temperature (BT) equal to 290 K and (b) BT double biases analysis for FY2E with IASI and AIRS sensors.

4. Satellite instrument parameters on-orbit optimizer (SIPOn-Opt) for FY3

Satellite data suffer from various error sources due to factors such as the special detecting mode of the instrument in space and uncertainties in the radiative transfer modeling and calibration. Figure 14 shows the major sources of observation and simulation errors in satellite data assimilation. Observation and simulation can both be biased. Observations are biased mostly by calibration (observed anomaly of cold space and warm load), nonlinearity of the instrument, and space environment contamination. Simulation is biased because of two factors: 1) errors in the atmospheric profile (such errors are determined mainly by numerical forecast uncertainty) and 2) errors in the simulation of the line-by-line (LBL) radiative transfer. There are two reasons for such errors: 1) observation errors of the absorption spectral lines used to build the LBL model and 2) the band-pass parameters of the instrument on-orbit, which are used in LBL modeling. These error sources are highly relevant to the performance of the instrument parameters on-orbit and have a significant influence on data quality. But these parameters cannot be measured exactly due to various constraints in ground measurement conditions or their change due to the influence of a different space environment after the satellite is launched. If these parameters can be exactly retrieved and properly used, the quality of data can be improved.

4.1 Summary of the algorithm

The SIPOn-Opt is designed to obtain more accurate performance parameters of the instrument in orbit. The variational inversion method is adopted in the optimization. The cost function J is the core of the algorithm, Δv_0 is the channel central frequency, bd is the bandwidth, stopband is the passband stop band, ΔT_{\max} is the nonlinearity, k is the antenna main beam efficiency, srf is the spectral response function, c is the abnormal cold space, w is the abnormal warm load, and a is the absorption line measurement error. In terms of the relevant parameters of universal instru-

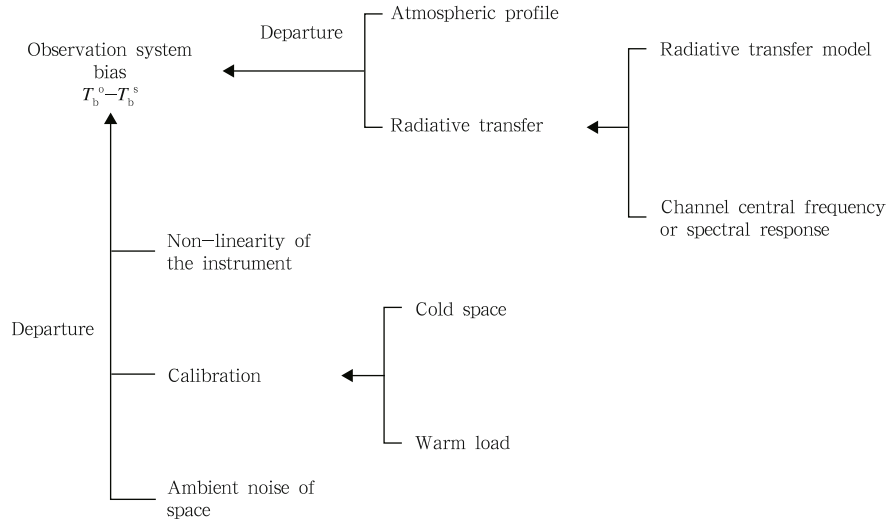


Fig. 14. The error terms, considered in the sensitivity study, that affect the departures (observed minus simulated brightness temperatures).

ments in orbit, Eq. (5) represents the cost function.

$$J(\Delta v_0, \text{bd}, \text{stopband}, \Delta T_{\max}, k, \text{srf}, c, w, a) = \frac{m(\Delta v_0, \text{bd}, \text{stopband}, \Delta T_{\max}, k, \text{srf}, c, w, a)}{\sigma_m^2} + \frac{s(\Delta v_0, \text{bd}, \text{stopband}, \Delta T_{\max}, k, \text{srf}, c, w, a)}{\sigma_s^2}, \quad (5)$$

where $m(\Delta v_0, \text{bd}, \text{stopband}, \Delta T_{\max}, k, \text{srf}, c, w, a)$ is the mean of the observation minus the simulation and $s(\Delta v_0, \text{bd}, \text{stopband}, \Delta T_{\max}, k, \text{srf}, c, w, a)$ is the standard deviation of the observation minus the simulation. These are the functions of the performance parameters of the instrument in orbit. The dynamic ranges of the mean and standard deviations σ_m and σ_s reflect the accuracy of the numerical prediction model. Errors by various instruments on-orbit propagate according to their own physical mechanisms (Lu et al., 2011b).

In terms of the FY3A/microwave temperature sounder (MWTS), after a sensitivity evaluation, we found that errors in the measured channel frequency and the nonlinearity of the instrument are the main sources of the observation system errors. Therefore, the cost function (Eq. (5)) can be simplified as

$$J(\Delta v_0, \Delta T_{\max}) = \frac{m(\Delta v_0, \Delta T_{\max})^2}{\sigma_m^2} + \frac{s(\Delta v_0, \Delta T_{\max})^2}{\sigma_s^2}. \quad (6)$$

Figure 15 represents a flow chart of the SIPOn-Opt. Based on the numerical analysis fields, real-time satellite instrumental observations, and constantly updated performance parameters of an instrument in orbit, radiometric calibration is carried out with observed BTs from the calibration and simulated BTs from radiative transfer modeling, and an optimal retrieval algorithm for the performance parameters of the instrument in orbit are developed by taking the mean and standard deviations of the observation minus simulation as a cost function. More accurate instrumental parameters on-orbit, such as channel central frequency, nonlinearity parameters, antenna main beam efficiency, and the spectral response function, can be optimally retrieved through this algorithm.

4.2 Application of SIPOn-Opt to the microwave temperature sounder of FY3

Most payloads in the first of China's second-generation polar-orbiting meteorological satellites were being launched for the first time. FY3A was the first in China's history to have quantitative assimilation ability. Four of FY3A's 11 instruments are of particular importance to numerical weather prediction, especially the MWTS. We take FY3A/MWTS as an example to demonstrate how the SIPOn-Opt detects and analyzes the dominant errors of the instru-

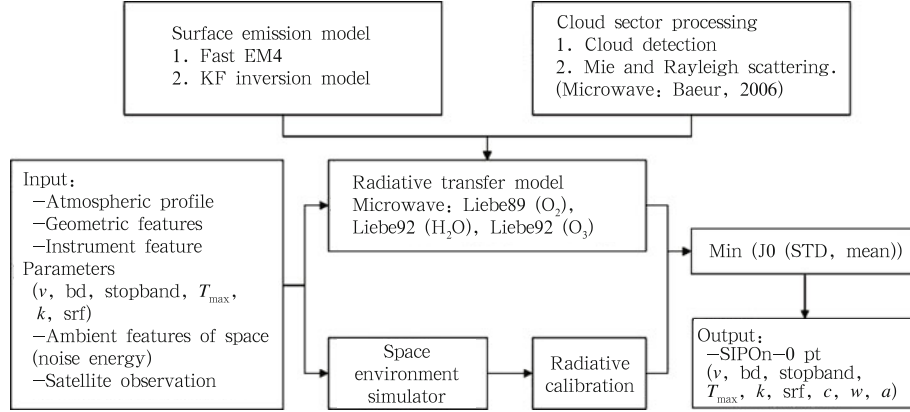


Fig. 15. Flow chart of the SIPOn-Opt, where v is the passband central frequency, bd is the passband width, stopband is the passband stop band, ΔT_{\max} is the nonlinearity, k is the antenna efficiency, srf is the spectral response function, c is the abnormal cold space, w is the abnormal warm load, and a is the absorption line measurement error.

ment, retrieves the satellite's performance parameters in orbit, corrects the observing system errors, and improves data quality. FY3A/MWTS is also assimilated by the world-leading ECMWF numerical forecast system to improve the model's forecast accuracy. After calculating and analyzing the sensitivity of the errors shown in Fig. 14 to the root-mean-square error between the observed and simulated values, we found the measurement errors of central frequency and nonlinearity to be the dominant sources of errors in FY3A/MWTS. More accurate parameters of central frequency and nonlinearity were then retrieved through SIPOn-Opt. Figure 16 shows global maps of the fit between the observed and simulated BTs of FY3A MWTS in comparison with that of the European Meteorological Operational satellite program-A/Advanced Microwave Sounding Unit-A (MetOp-A/AMSU-A). The BTs of FY3A MWTS are obtained through using more accurate channel frequencies and nonlinearity corrections including the designed central frequency, the measured frequency in the lab before launch, and nonlinearity parameters through variational optimization. When taking the satellite observation as a reference for comparison with the simulation results, if the observation physically fits the simulation well, the departure of the observation minus simulation follows a Gaussian distribution with a zero mean and a certain root-mean-square error.

Taking FY3A/MWTS Channel 4 as an example

(column 3 in Fig. 16), FY3A/MWTS Channel 4 and MetOp-A/AMSU-A Channel 9 have the same instrument design configuration. There is a 0.5-h difference between the two satellites' overpass of the same location, and the observing objects are concentrated in an atmosphere of 100 hPa. In this case, the departures between the observations and simulations of the two should be consistent, but there is a large difference in the designed central frequency, as shown in Fig. 16. We can see that this departure has been improved after calculation with the lab measurement parameters before the satellite is launched, but it is still large. After analyzing the sensitivity of the errors, we found that the data quality and the departure were affected by the measurement error of the channel central frequency and the nonlinear effect. The measurement frequency bias is because of the use of Gunn diode frequency lock technology. We theorize that the channel frequency locks a vibration within a resonator. This locked channel frequency is affected by the resonator's environment. The atmospheric environment in the lab is different from the vacuum environment in outer space, and this leads to their different measurement channel frequencies. By comparing the departure histograms, we see that the departure is improved after the frequency bias is corrected, but there is still a positive bias of about 1 K. Satellite remote sensing uses radiometers to measure an object, assuming a linear relationship between the electric signal and

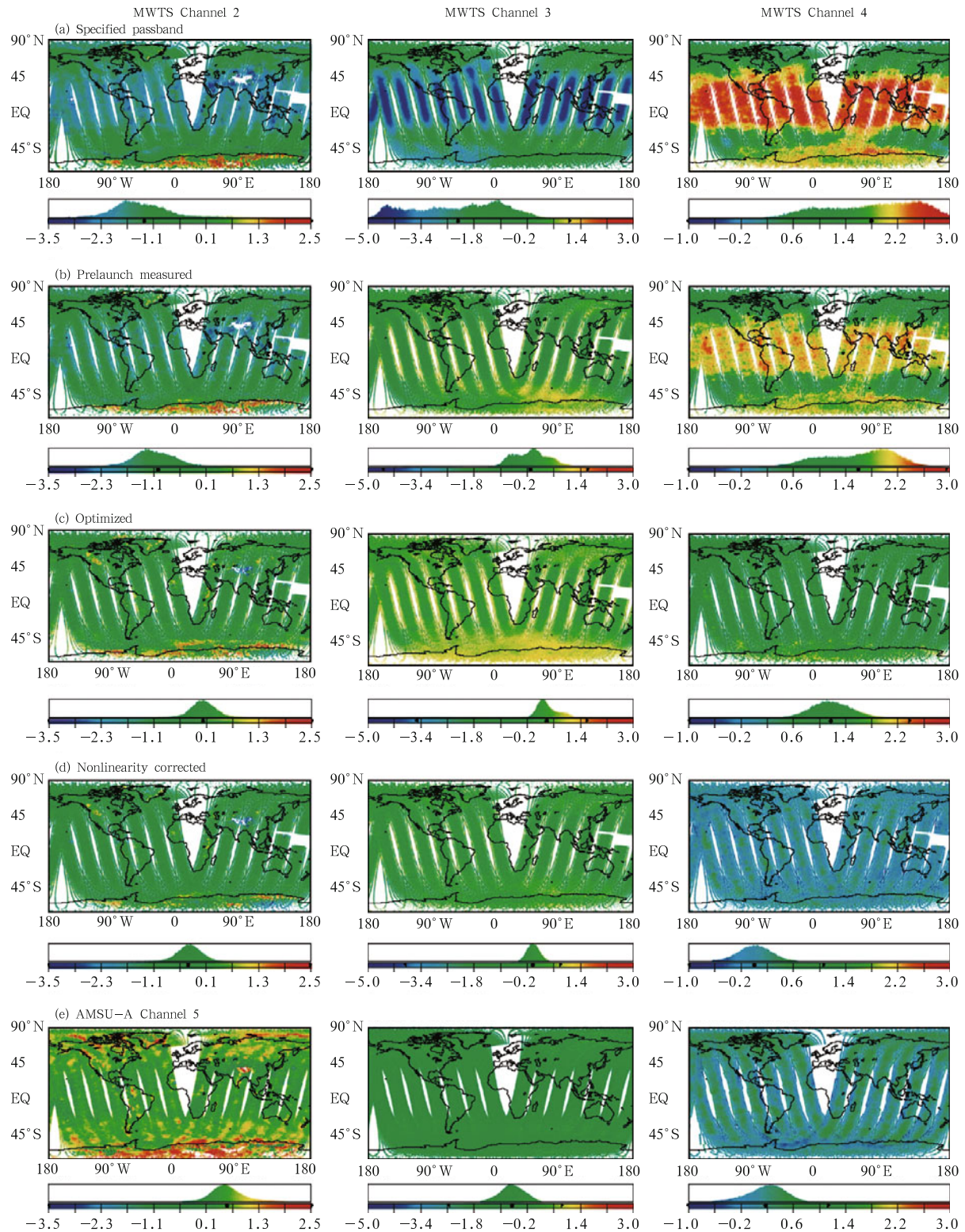


Fig. 16. Maps of first-guess BT departures (K) for MWTS channels 2–4 (from left to right) by using (a) design-specified passbands, (b) prelaunch-measured passbands, (c) optimized passbands, (d) passbands following nonlinearity correction, and (e) the corresponding equivalent MetOp-A first-guess departure maps. The spots at the base of the histograms indicate the mean first-guess departure. [From Lu et al., 2011b]

the object's energy. It then adopts a two-point linear calibration. In fact, there is a certain nonlinear effect in radiometers. The simulated departure can be comparable to that of the AMSU-A when the nonlinear effect is also corrected.

In summary, Figs. 16a–d demonstrate that departures of MWTS channels 2–4 are subject to a Gaussian distribution of zero mean and a smaller root-mean-square error after the frequency bias and nonlinear effect are corrected. The result is more comparable to (even better than) the results of the AMSU-A (Fig. 16e). When corrected FY3A/MWTS data are applied to the ECMWF assimilation/prediction system, prediction skill is improved by 1% in the Southern Hemisphere (Lu et al., 2012).

The correction algorithm of the frequency measurement error and the nonlinear radiative effect were implemented in the operational preprocessing system of the FY3A/MWTS at the National Satellite Meteorological Center (NSMC) of the China Meteorological Administration (CMA) in March 2011. Thereafter, the error of the simulated root-mean-square departure is about 0.2 K, which is comparable to that of the MetOp-A/AMSUA. The corrected data are released to the public domain by the NSMC of the CMA.

The module for correcting frequency measurement errors and nonlinear radiative effects, similar to that of the FY3A MWTS, has also been implemented in the FY3B's MWTS operational preprocessing system. Therefore, in terms of the FY3B MWTS, these two errors are not dominant. In fact, scanning angle biases related to the scanning position are the dominant biases, which can be corrected through a bias correction algorithm in the assimilation system.

FY3C was launched successfully in September 2013. Currently, it is in the on-orbit testing phase. SIPOn-Opt is being used to detect and correct the dominant observing system biases to further improve data quality.

5. Summary

The innovations to the algorithms discussed above are summarized as follows:

(1) The traditional image navigation technique depends on landmark matching, while the FY2 image navigation technique uses vectors pointing at the earth disk center. The latter technique not only draws the outline of the navigation equation more clearly but also more easily achieves an accurate input parameter. In the traditional image navigation technique, the β angle is expressed in an empirical formula, while the FY2 image navigation technique uses an analytic expression. Advanced coordinate systems ensure the quality of solutions to the image navigation equations.

(2) Before 2012, FY2 geostationary meteorological satellites mainly used inter-calibration with other satellites for operational calibration processing. However, the calibration timeline (7–15 days) and accuracy (2–3 K) needed to be improved due to the temporal, spectral, and spatial differences between different sensors. By using CIBLE, two main difficulties have been conquered. First, by correcting the radiometric contributions of the FCCs, hourly high frequency calibration in the IR bands has been realized with the IBB observations, which had previously only been used for on-orbit monitoring of radiometric stability. Second, the on-orbit observed IR radiance from the lunar surface is used to correct the systematic error of the IBBC, which results in the realization of highly frequent (hourly), high accuracy (less than 1 K) IR radiometric calibration.

(3) It has been assumed that the instruments in a meteorological satellite on-orbit are consistent with their design specifications, that the instrumental performance parameters on-orbit are consistent with the values measured before the satellite is launched, and that even if certain differences exist, there is no effective way to calculate such values. However, practical applications show that these parameters do vary and that these variations have an impact on data quality and on the effectiveness of their application to numerical weather prediction. For the first time, an SIPOn-Opt has been developed and used to variationally retrieve the performance parameters of instruments on-orbit. More exact instrumental parameters can be retrieved through such observation constraints as the channel central frequency, nonlinear parameters, the

antenna main-beam efficiency, and the spectral response function. These parameters may be used to correct satellite observation system biases, making the data of FY3 consistent with its counterparts from the European and the U.S. space agencies. When the data of FY3 are assimilated with the ECMWF model, the prediction accuracy of the model is also improved. When this model is used in meteorological satellite instruments (MSU and AMSU-A) from Europe and the U.S., the quality and effectiveness of the data from these instruments, applied over the past 40 years, are also improved.

REFERENCES

- Bauer, P., E. Moreau, F. Chevallier, et al., 2006: Multiple-scattering microwave radiative transfer for data assimilation applications. *Quart. J. Roy. Meteor. Soc.*, **132**, 1259–1281.
- Guo Qiang, Chen Boyang, Yang Changjun, et al., 2012: On-orbit radiometric calibration for water-vapor band for FY-2 satellite. *Journal of Infrared Millimeter Waves*, **31**, 523–527. (in Chinese)
- , —, Zhang Yong, et al., 2013: Progress in on-orbit radiometric calibration technology for Fengyun-2 satellite. *Adv. Meteor. Sci. Technol.*, **3**, 6–12. (in Chinese)
- Hambrick, L. N., and D. R. Phillips, 1980: Earth locating image data of spin-stabilized geosynchronous satellites. NOAA Tech. Memo., NESDIS 111, 105 pp.
- Lu, F., X. H. Zhang, and J. M. Xu, 2008: Image navigation for the FY2 geosynchronous meteorological satellite. *J. Atmos. Oceanic Technol.*, **25**, 1149–1165.
- Lu, Q. F., W. Bell, P. Bauer, et al., 2011a: An evaluation of FY-3A satellite data for numerical weather prediction. *Quart. J. Roy. Meteor. Soc.*, **137**, 1298–1311.
- , —, —, et al., 2011b: Characterizing the FY-3A microwave temperature sounder using the ECMWF model. *J. Atmos. Oceanic Technol.*, **28**, 1373–1389.
- , —, —, et al., 2012: Improved assimilation of data from China's FY-3A microwave temperature sounder (MWTS). *Atmos. Sci. Lett.*, **13**, 9–15.
- , and —, 2014: Characterizing channel center frequencies in AMSU-A and MSU microwave sounding instruments. *J. Atmos. Oceanic Technol.*, **31**, 1713–1732.
- Xu Jianmin, Niu Yenseng, Dong Chaohua, et al., 2006: Ground segments for FY meteorological satellites. *Engineering Sciences*, **8**, 13–18, 24 and Cover 3. (in Chinese)